AAS 11-464

CURVILINEAR COORDINATES FOR COVARIANCE AND RELATIVE MOTION OPERATIONS

David A. Vallado[*], and Salvatore Alfano[†]

Relative motion studies have traditionally focused on linearized equations, and inserting additional force models into existing formulations to achieve greater fidelity. A simpler approach may be numerically integrating the two satellite positions and then converting to a modified equi-distant cylindrical frame as necessary. Recent works have introduced some approaches for this transformation as it applies to covariance operations, with some approximations. We develop an exact transformation between Cartesian and curvilinear frames and test the results for various orbital classes. The transformation has applicability to covariance operations which we also introduce. Finally, we examine how the transformation affects graphical depiction of the covariance matrix.

INTRODUCTION

Relative motion studies have traditionally focused on linearized equations, and inserting additional force models into existing formulations to achieve greater fidelity. For very close proximity operations, this is reasonable and has been in use for many decades. Some studies use a Hills frame for large satellite displacements and this may not be accurate. A simpler approach for a wide range of satellite displacements is to numerically integrate the two satellite positions and then convert to a Hills frame as necessary. Recent literature has introduced some approaches for this transformation as it relates to covariance matrices, with some approximations. We develop an exact transformation between Cartesian and curvilinear frames and test the results for various orbital classes. The transformation has applicability to covariance operations which we also investigate. Finally, we examine how the transformation affects depiction of the covariance matrix. A summary is below.

- Characterize the accuracy of the transformation between Cartesian and a modified Equidistant Cylindrical space (Weisstien 2011) (expected sub meter level) for both position and velocity vectors. This includes exercising the transformation in both directions.
- Quantify and qualify the ability of the transformation to work on various orbital types (LEO, MEO, HEO, GEO, etc). We will analyze the operating envelope of the technique by plotting the error of the traditional Hills technique for both position and velocity vectors.
- Document the improvement in accuracy from traditional Hills solutions for each case – quantify the error introduced by Hills solutions for larger satellite separations. We will do this for full force model configurations.

Finally, we examine implications for visualization of the covariance matrix, and relative motion solutions.

[*] Senior Research Astrodynamicist, Analytical Graphics Inc., Center for Space Standards and Innovation, 7150 Campus Dr., Suite 260, Colorado Springs, Colorado, 80920-6522. dvallado@agi.com
[†] Senior Research Astrodynamicist, Analytical Graphics Inc., Center for Space Standards and Innovation, 7150 Campus Dr., Suite 260, Colorado Springs, Colorado, 80920-6522. salfano@agi.com

Previous studies have introduced curvilinear transformations (Hill, Alfriend, and Sabol, 2008), although they focused on the covariance propagation and orbital element aspects. We do not investigate the propagation behavior of the covariance matrix and any effects of generation via Cartesian vectors or orbital element sets. Rather, we focus on the single point in time curvilinear transformation and reverse method, including velocity vectors. The two approaches should be complimentary.

TRANSFORMATION PROCESS

The *xyz* system normally used for relative motion can be misleading in its portrayal of the actual relative differences. The *x* component is the same in both systems, but the *y* and *z* components contain differences due to the curvilinear motion. Consider an interceptor satellite whose displacement relative to the target satellite has only *y* and *z* axis components, when expressed in the relative (Hill's) frame. The traditional Hills coordinate system is shown in Fig. 1. Note that we use a target and interceptor notation where the interceptor is displaced from the target. For our applications, the interceptor represents either the other satellite that is close to the target (relative motion), or points on the instantaneous covariance about a target satellite (covariance).

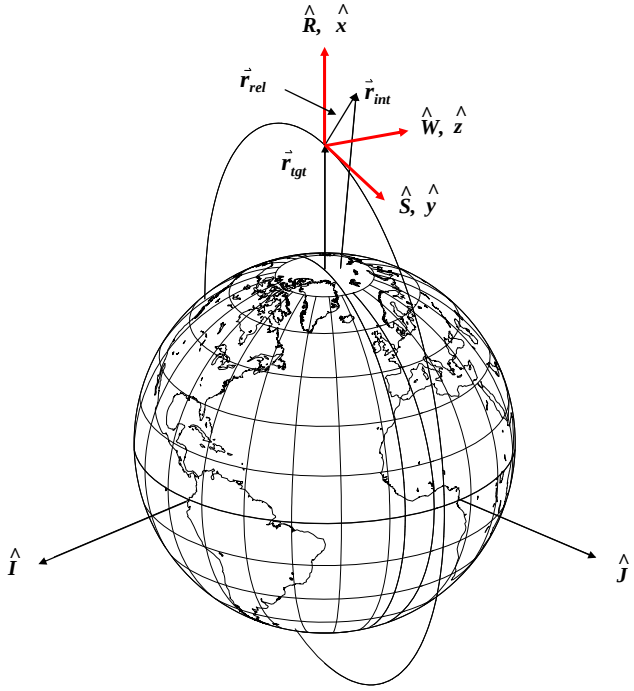

Figure 1 Hills Coordinate System. The traditional Hills coordinate system aligns with the RSW system as shown. Displacements *x, y* and *z* and their rates describe the displacements between the target and interceptor vehicles.

Figure 2 shows that this displacement actually has an *x* component as well, due to the curvature of the target satellite's orbit (e.g. a *y* displacement of 100 m is really slightly less than 100 m, and have a small negative *x* component).

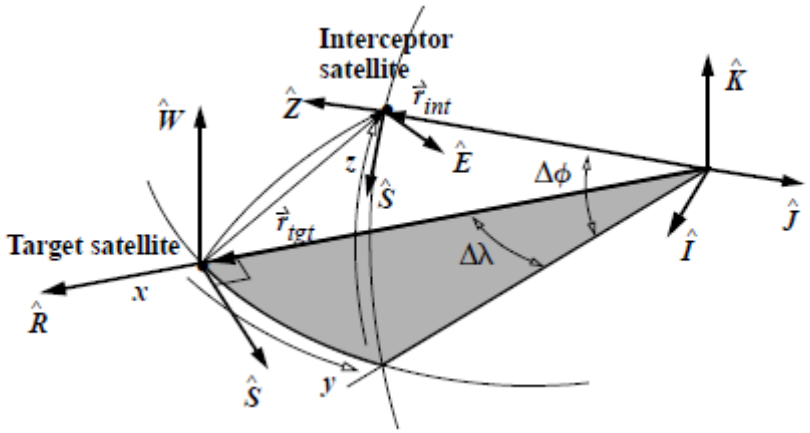

Figure 2 Relative Position of Interceptor and Target. This diagram is extremely exaggerated to illustrate the inconsistency in assuming the Hill's *y* and *z* component displacements transfer directly to Cartesian position and velocity vectors.

The question we must address is how to convert between frames—between the true vector positions, and the linearized, or relative Hill's-like equation positions. Because we also examine eccentric orbits, we modify the ***Equidistant Cylindrical*** (EQC) system (Weisstein, 2011). This system, possibly developed by Eratosthenes about 250 BC, has equal distances for polar and equatorial mappings. Using a central meridian of λ_o, the following equations apply. The reverse formulae are also given.

$$x = \lambda - \lambda_o \text{ and } \lambda = \lambda_o + x \sec(\phi)$$
$$y = \phi \tag{1}$$

We derive two transformations because for perfectly circular orbits, the RSW frame properly represents the displacements from the target satellite. The technique is derived using the EQC frame and is valid for all perfectly circular orbits. It can be used to establish the uncertainty in using Hill's equations for relative motion, and the positional displacements you would expect for various orbits. Obtaining the correct velocity components is an important aspect, and it is why we chose the EQC frame.

Elliptical orbits require a slightly different formulation because the arc length (the *y* distance shown in Fig. 2) is actually a function of the true anomaly. We noticed this while examining the eccentric orbit test cases, especially the Molnyia (e = 0.7) satellite. Although the EQC system appears to solve the problem, the distance in an elliptical orbit between two true anomaly values introduces an arc length dependency that ultimately requires an elliptic integral (as suggested by Hill, Alfriend, and Sabol, 2008). Therefore, we use a modified EQC (EQCM) notation for the coordinate system, in which we bend the frame about the target orbital path (because the uncertainty will be largest in this direction). This requires the NTW coordinate system (Vallado 2007;165) instead of the usual RSW frame.

To derive the transformations, we examine a case in which we know the target's position and velocity in Earth Centered Inertial space (ECI) and the relative interceptor position and velocity in the rotating EQCM frame. (Note that for circular orbits, this will be the traditional Hills frame) To determine the interceptor position and velocity vectors in the inertial frame, we perform a series of calculations starting from the target inertial position. Recognize that for the *y* and *z* directions, the EQCM frame lies in a curved frame in inertial space. We interchangeably use a state vector notation where $\boldsymbol{X}$ is composed of the position and velocity vectors ($\vec{r}, \vec{v}$).

Determining the velocity requires careful work. A benefit of using the EQCM frame is that the relations are more easily found for both cases (circular and eccentric). Figure 3 is needed for the formulation.

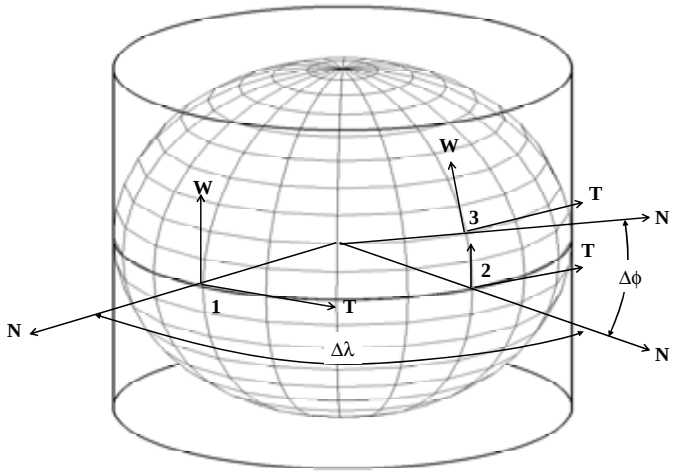

Figure 3 Elliptical Orbit Transformation. Transforming the coordinates between the target (1) and interceptor (3) requires several intermediate positions. Notice that the Earth is stretched to highlight the differences when using elliptical orbits.

The exaggeration of the sphere is because the arc length cannot be related simply by a range and angular separation ($s = r\theta$) due to the nature of the elliptical orbit.

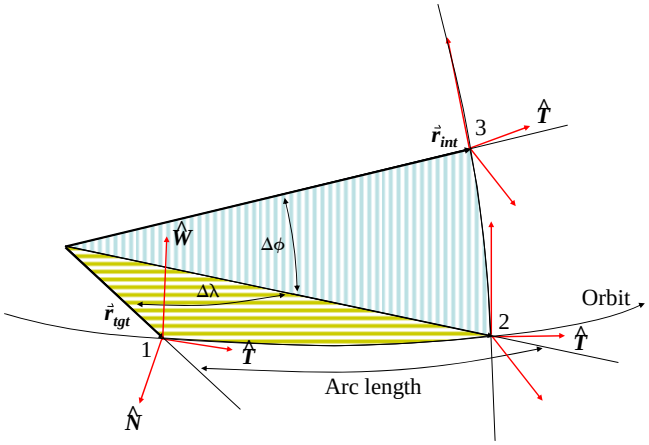

Figure 4 Arc Length Determination. Transforming the coordinates requires angles and rates of change. The various positions (1, 2, and 3) are shown in the transformation, ranging from the target (1) to the interceptor (3). The figure is exaggerated to indicate the effect and geometry of an eccentric orbit.

For circular orbits, the transformation is found using Fig. 3 (which would have no distortion for circular orbits). Here we use the EQC notation because it is compatible with the Hills frame. The RSW to SEZ transformation is used in both transformations.

$$\left[\frac{RSW}{SEZ}\right] = \begin{bmatrix} \sin(\Delta\phi)\cos(\Delta\lambda) & -\sin(\Delta\lambda) & \cos(\Delta\phi)\cos(\Delta\lambda) \\ \sin(\Delta\phi)\sin(\Delta\lambda) & \cos(\Delta\lambda) & \cos(\Delta\phi)\sin(\Delta\lambda) \\ -\cos(\Delta\phi) & 0 & \sin(\Delta\phi) \end{bmatrix} \tag{2}$$

$$
\begin{aligned}
&EQC2ECI(\left[X_{tgt}\right]_{ECI}, x, y, z, \dot{x}, \dot{y}, \dot{z} \longrightarrow \left[X_{int}\right]_{ECI}) \\
&\left[X_{tgt}\right]_{ECI} \longrightarrow \left[\hat{R} \mid \hat{S} \mid \hat{W}\right] \\
&\Delta\lambda = \frac{y}{r_{tgt}} \qquad \Delta\phi = \frac{z}{r_{tgt}} \qquad \Delta\dot{\lambda}_{tgt} = \frac{\vec{v}_{tgt_{RSW}}(s)}{r_{tgt}} \\
&\Delta\dot{\lambda}_{int} = \frac{\dot{y}}{r_{tgt}} + \Delta\dot{\lambda}_{tgt} \qquad \Delta\dot{\phi}_{int} = \frac{\dot{z}}{r_{tgt}} \qquad r_{int} = \left|\vec{r}_{tgt}\right| + x \\
&\vec{v}_{int_{SEZ}} = \begin{bmatrix} -r_{int}\Delta\dot{\phi}_{int} \\ r_{int}\Delta\dot{\lambda}_{int}\cos(\Delta\phi) \\ \dot{x} + \vec{v}_{tgt_{RSW}}(r) \end{bmatrix} \qquad \vec{v}_{int_{RSW}} = \left[\frac{RSW}{SEZ}\right]\vec{v}_{int_{SEZ}} \\
&\vec{r}_{int_{RSW}} = \begin{bmatrix} r_{int}\cos(\Delta\phi)\cos(\Delta\lambda) \\ r_{int}\cos(\Delta\phi)\sin(\Delta\lambda) \\ r_{int}\sin(\Delta\phi) \end{bmatrix} \\
&\left[X_{int}\right]_{ECI} = \left[\hat{R} \mid \hat{S} \mid \hat{W}\right]\left[X_{int}\right]_{RSW}
\end{aligned}
\tag{3}
$$

The reverse process uses similar formulae.

$$
\begin{aligned}
&ECI2EQC(\left[X_{tgt}\right]_{ECI}, \left[X_{int}\right]_{ECI} \longrightarrow x, y, z, \dot{x}, \dot{y}, \dot{z}) \\
&\left[X_{tgt}\right]_{ECI} \longrightarrow \left[\hat{R} \mid \hat{S} \mid \hat{W}\right] \\
&\left[X_{tgt}\right]_{RSW} = \left[\hat{R} \mid \hat{S} \mid \hat{W}\right]^{T}\left[X_{tgt}\right]_{ECI} \\
&\left[X_{int}\right]_{RSW} = \left[\hat{R} \mid \hat{S} \mid \hat{W}\right]^{T}\left[X_{int}\right]_{ECI} \\
&\Delta\lambda = a\tan 2(\vec{r}_{int_{RSW}}(s), \vec{r}_{int_{RSW}}(r)) \\
&\Delta\phi = \sin^{-1}\left(\frac{\vec{r}_{int_{RSW}}(w)}{r_{int}}\right) \qquad \Delta\dot{\lambda}_{tgt} = \frac{\vec{v}_{tgt_{RSW}}(s)}{r_{tgt}} \\
&\vec{r}_{int_{EQC}} = \begin{bmatrix} r_{int} - r_{tgt} \\ r_{tgt}\Delta\lambda \\ r_{tgt}\Delta\phi \end{bmatrix} = \begin{bmatrix} x \\ y \\ z \end{bmatrix} \\
&\vec{v}_{int_{SEZ}} = \left[\frac{RSW}{SEZ}\right]^{T}\vec{v}_{int_{RSW}} \\
&\Delta\dot{\lambda}_{int} = \frac{\vec{v}_{int_{SEZ}}(e)}{r_{int}\cos(\Delta\phi)} \qquad \Delta\dot{\phi}_{int} = \frac{-\vec{v}_{int_{SEZ}}(s)}{r_{int}\cos(\Delta\phi)} \\
&\vec{v}_{int_{EQC}} = \begin{bmatrix} \vec{v}_{int_{SEZ}}(z) - \vec{v}_{tgt_{RSW}}(r) \\ r_{tgt}\left(\Delta\dot{\lambda}_{int} - \Delta\dot{\lambda}_{tgt}\right) \\ r_{tgt}\Delta\dot{\phi}_{int} \end{bmatrix} = \begin{bmatrix} \dot{x} \\ \dot{y} \\ \dot{z} \end{bmatrix}
\end{aligned}
\tag{4}
$$

The transformation process for elliptical orbits has several steps as well, but we have to transform the vectors into the NTW coordinate frame. In Fig. 3 and 4, this is point 1. Next, we setup latitude and longitude-like transformations to relate the interceptor to the target (point 2 in Fig. 3). Finally, we rotate to a NTW frame centered at the interceptor position to find the solution. The challenge is finding the arc length from the true anomaly (and reverse).

First convert the vector to the NTW frame.

$$
\begin{aligned}
&ECI2EQCM(\left[X_{tgt}\right]_{ECI},\left[X_{int}\right]_{ECI} \longrightarrow x, y, z, \dot{x}, \dot{y}, \dot{z}) \\
&\left[X_{tgt}\right]_{ECI} \longrightarrow \left[\hat{N} \mid \hat{T} \mid \hat{W}\right] \\
&\left[X_{tgt}\right]_{NTW} = \left[\hat{N} \mid \hat{T} \mid \hat{W}\right]^{T} \left[X_{tgt}\right]_{ECI} \\
&\left[X_{int}\right]_{NTW} = \left[\hat{N} \mid \hat{T} \mid \hat{W}\right]^{T} \left[X_{int}\right]_{ECI}
\end{aligned}
\tag{5}
$$

Then find the rotation angles.

$$
\begin{aligned}
&\Delta\lambda_{tgt} = a\tan 2(\vec{r}_{tgt_{NTW}}(n), \vec{r}_{tgt_{NTW}}(w)) \\
&\Delta\lambda_{int} = a\tan 2(\vec{r}_{int_{NTW}}(n), \vec{r}_{int_{NTW}}(w)) \\
&\phi_{int} = \sin^{-1}\left(\frac{\vec{r}_{int_{NTW}}(t)}{r_{int}}\right)
\end{aligned}
\tag{6}
$$

Both approaches require the orbital elements. Following notation of classical orbital elements of Vallado (2007:104), note that the eccentricity unit vector is the direction of perigee. If it doesn't exist below some tolerance, it's set to be the target unit vector.

$$
\begin{aligned}
&\vec{h}_{tgt} = \vec{r}_{tgt_{NTW}} \times \vec{v}_{tgt_{NTW}} \\
&p_{tgt} = \frac{h_{tgt}^{\ 2}}{\mu} \\
&\vec{e}_{tgt} = \frac{\vec{v}_{tgt_{NTW}} \times \vec{h}_{tgt}}{\mu} - \frac{\vec{r}_{tgt_{NTW}}}{r_{tgt}} \\
&a_{tgt} = \frac{p_{tgt}}{1 - e_{tgt}^{\ 2}} \\
&if \;\; e > 0.00001 \\
&\qquad \hat{e} = \frac{\vec{e}_{tgt}}{e} \\
&\quad else \\
&\qquad \hat{e}_{tgt} = \frac{\vec{r}_{tgt_{NTW}}}{r_{tgt}}
\end{aligned}
\tag{7}
$$

The arc parameters are found next.

$$
\begin{aligned}
&\lambda_{perigee} = a\tan 2(\vec{e}_{tgt}(t), \vec{e}_{tgt}(n)) \\
&\nu_{start} = \Delta\lambda_{tgt} - \lambda_{perigee} \\
&\nu_{end} = \Delta\lambda_{int} - \lambda_{perigee}
\end{aligned}
\tag{8}
$$

Both approaches need the equivalent target positions at point 2 in Fig. 3 and 4. Here, we use the Perifocal Coordinate system (PQW, Vallado 2007: 162-163.)

$$
\begin{aligned}
r_{2tgt} &= \frac{p_{tgt}}{1+e\cos(\nu_{end})} \\
\hat{P} &= \hat{e} \\
\hat{Q} &= [0 \quad 0 \quad 1] \times \hat{P} \\
\vec{r}_{2tgt_{NTW}} &= r_{2tgt}\left(\cos(\nu_{end})\hat{P} + \sin(\nu_{end})\hat{Q}\right) \\
\vec{v}_{2tgt_{NTW}} &= -\sqrt{\frac{\mu}{p_{tgt}}}\left(\sin(\nu_{end})\hat{P} + \left(e+\cos(\nu_{end})\right)\right)\hat{Q}
\end{aligned}
\tag{9}
$$

Next, adjust the NTW positions to the interceptor location. This is point 3 in Fig. 3 and 4. For the arc length calculation, we opted for a simple numerical routine rather than a full elliptic integral. Our comparison tests show this approach matches complete elliptical integrals to $1\text{x}10^{-7}$m.

$$
\begin{aligned}
&\left[\vec{r}_{2tgt} \; \vec{v}_{2tgt}\right]_{ECI} \longrightarrow \left[\hat{N} \mid \hat{T} \mid \hat{W}\right] \\
&\left[\vec{r}_{2tgt} \; \vec{v}_{2tgt}\right]_{NTW} = \left[\hat{N} \mid \hat{T} \mid \hat{W}\right]^T \left[\vec{r}_{2tgt} \; \vec{v}_{2tgt}\right]_{ECI} \\
&[\phi] = rot2(\phi_{int}) \\
&\left[X_{3int}\right]_{NTW} = [\phi]\left[\hat{N} \mid \hat{T} \mid \hat{W}\right]^T \left[X_{int}\right]_{ECI} \\
&temp1 = elliptical\ arc\ length\ \ from\ true\ anomalies \\
&\vec{r}_{int_{EQCM}} = \begin{bmatrix} \vec{r}_{3int_{NTW}}(n) - \vec{r}_{2tgt_{NTW}}(n) \\ temp1 \\ \phi_{int} r_{2tgt} \end{bmatrix} = \begin{bmatrix} x \\ y \\ z \end{bmatrix} \\
&\vec{v}_{int_{EQCM}} = \begin{bmatrix} \vec{v}_{3int_{NTW}}(n) - \vec{v}_{tgt_{NTW}}(n) \\ \vec{v}_{3int_{NTW}}(t) - \vec{v}_{2tgt_{NTW}}(t) \\ \vec{v}_{3int_{NTW}}(w) \end{bmatrix} = \begin{bmatrix} \dot{x} \\ \dot{y} \\ \dot{z} \end{bmatrix}
\end{aligned}
\tag{10}
$$

We programmed these in Matlab as eci2eqcm.m.

The reverse process is similar, but it has several subtleties and is presented separately. To find the components and rates in the EQCM frame, begin with the following.

$$
\begin{aligned}
&EQCM\,2ECI(\left[X_{tgt}\right]_{ECI}, x, y, z, \dot{x}, \dot{y}, \dot{z} \longrightarrow \left[X_{int}\right]_{ECI}) \\
&\left[X_{tgt}\right]_{ECI} \longrightarrow \left[\hat{N} \mid \hat{T} \mid \hat{W}\right] \\
&\left[X_{tgt}\right]_{NTW} = \left[\hat{N} \mid \hat{T} \mid \hat{W}\right]^T \left[X_{tgt}\right]_{ECI}
\end{aligned}
\tag{11}
$$

Then find the orbital elements as in Eq. 7. The angles are found next.

$$
\begin{aligned}
\Delta\lambda_{tgt} &= a\tan 2(\vec{r}_{tgt_{NTW}}(t), \vec{r}_{tgt_{NTW}}(n)) \\
\lambda_{perigee} &= a\tan 2(\vec{e}_{tgt}(t), \vec{e}_{tgt}(n)) \\
\nu_{start} &= \Delta\lambda_{tgt} - \lambda_{perigee}
\end{aligned}
\tag{12}
$$

The ending true anomaly is also found using numerical routines. This step inserts an assumption that the covariance does not extend to more than ½ an orbit. Additional work could be done to use elliptic integrals and advanced techniques, but the usefulness is limited and any operation seeking to determine probability calculations would find an answer with extremely low probability – the satellite is uncertain to within ½ an orbital revolution! Again, the routines show excellent comparison to rigorous techniques. This enables us to find

$$\Delta\lambda_{int} = \nu_{end} + \lambda_{perigee} \tag{13}$$

The next step is to form the PQW vectors as in Eq 9. We find a secondary transformation of the target vector at position 2.

$$\begin{aligned}
&\left[X_{2tgt}\right]_{ECI} \longrightarrow \left[\hat{N}\,|\,\hat{T}\,|\,\hat{W}\right] \\
&\left[X_{3tgt}\right]_{NTW} = \left[\hat{N}\,|\,\hat{T}\,|\,\hat{W}\right]^{T}\left[X_{2tgt}\right]_{ECI} \\
&\phi_{int} = \sin^{-1}\left(\frac{z}{r_{2tgt_{NTW}}}\right) \\
&\vec{r}_{int_{NTW}} = \begin{bmatrix} \cos(\phi_{int})\cos(\Delta\lambda_{int}) \\ \cos(\phi_{int})\sin(\Delta\lambda_{int}) \\ \sin(\phi_{int}) \end{bmatrix}
\end{aligned} \tag{14}$$

Find the final position and velocity displacements.

$$\begin{aligned}
&[\phi] = ROT2(\phi_{int}) \\
&\vec{v}_{3int_{ECI}} = \begin{bmatrix} \dot{x} + \vec{v}_{tgt_{NTW}}(n) \\ \dot{y} + \vec{v}_{2tgt_{NTW}}(t) \\ \dot{z} \end{bmatrix} \\
&\vec{v}_{2int_{ECI}} = [\phi]\left[\hat{N}\,|\,\hat{T}\,|\,\hat{W}\right]_2^T \vec{v}_{3int_{ECI}} \\
&\vec{v}_{int_{ECI}} = \left[\hat{N}\,|\,\hat{T}\,|\,\hat{W}\right]_1^T \vec{v}_{2int_{ECI}} \\
&\vec{r}_{3int_{NTW}} = [\phi]\left[\hat{N}\,|\,\hat{T}\,|\,\hat{W}\right]_2^T \vec{r}_{int_{NTW}} \\
&\vec{r}_{3uint_{NTW}}(n) = x + \vec{r}_{2tgt_{NTW}}(n) \\
&r_{scale} = \frac{\vec{r}_{3int_{NTW}}(n)}{\vec{r}_{3uint_{NTW}}(n)} \\
&\vec{r}_{1int_{NTW}} = r_{scale}\vec{r}_{int_{NTW}} \\
&\vec{r}_{int_{ECI}} = \left[\hat{N}\,|\,\hat{T}\,|\,\hat{W}\right]_1^T \vec{r}_{1int_{NTW}}
\end{aligned} \tag{15}$$

We programmed these in Matlab as eqcm2eci.m.

RESULTS

Several comparisons and analyses are possible. We can examine each position and velocity component variation from a single initial starting point displacement. We can vary the initial displacement. A compre-

hensive set of graphs would require a lot of space to cover so the following figures are intended only to give an indication of the magnitudes of differences you may experience.

Hill's equations are often used to study proximity flight and operations, usually from circular or near-circular orbits. The assumptions used in Hill's formulation clearly introduce error into the solution. Yet they are still widely used for initial planning. Additional realism may be inserted by using the perturbed equations of motion, but the underlying errors still remain.

We examine two-body and perturbed cases. The perturbed cases use "complete" force models. For instance, for the LEO satellites, we used a 70 × 70 gravitational model, NRL-MSIS00 drag, tides, solar radiation pressure, third body. For the GEOs, we reduced the gravity field size and did not include tides and atmospheric drag. In comparison, other authors have extended Hill's equations into perturbed motion (Schweighart and Sedwick, 2002). This is most often accomplished by adding the perturbing forces to the traditional Hills equations (Vallado, 2007:397) which can become quite complex.

There are several factors that affect the resulting curves, and we wish to establish the performance of the curvilinear transformation for various orbital types (LEO, MEO, HEO, GEO), and for positional and velocity differences. Cases ere tested for 10, 100, and 1000 m positional differences, and 0.01, and 0.1 m/s differences. We examine each axis individually, then all axes together with the same value. Because position and velocity differences will affect the orbit differently, we applied each velocity error to each positional choice, resulting in 6 possible combinations for each satellite orbit.

Examining the vectors that we can propagate, Fig. 5 shows the propagation and comparisons to make.

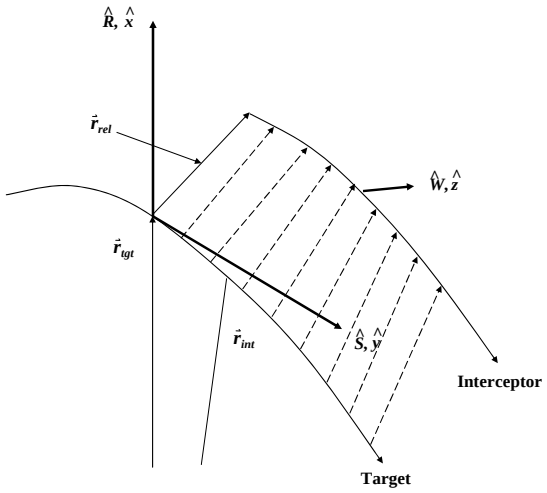

Figure 5 Initial Setup Processing. The setup uses the target Cartesian position and velocity vectors and the initial displacement (sometimes in the Hill frame, sometimes in the EQC frame) depending on the eccentricity. Both ECI vectors are propagated and the difference (in ECI) is converted to an equivalent Hills-like representation for comparison to a traditional Hills propagation.

To understand the ability of the transformation to properly model the motion and compare with the traditional Hills results, we first form the interceptor vector using the hills2eci.m. This takes the target position and velocity vectors along with the Hills displacement and forms the interceptor Cartesian vectors. The two Cartesian states are then propagated with a numerical integrator while the Hills equation is simply solved to create an ephemeris of displacements from the target satellite. The propagated target and interceptor states are then converted back to Hills space at each step. The calculated Hills (from the numerical vectors) is then differenced from the traditional Hills propagation. This comparison reveals the differences between the two approaches, and ultimately, the error in the linearization of the Hills frame.

We modify the process when examining near-circular orbits, or highly eccentric orbits. In these cases, we use the EQCM transformation because of the eccentricity component and it is used to find the interceptor initial state. The two Cartesian vectors are then used to find what an equivalent Hills initial displacement would be, noting that there is uncertainty here because Hills space is not truly defined for non-circular orbits. In the first few cases, we examine only near circular orbits with small eccentricities, as opposed to the 0.0 eccentricity in the first set of test cases.

Begin by considering an initial case where the orbit is in a nominal LEO, circular 500 km altitude orbit. We examine just the 1000 m and .1 m/s initial displacement condition. The positional differences are shown in Fig. 6. Note that the along-track component exhibit's the majority of the error. The magnitude is in blue, and represents the overall difference. The error bars approximate the error uncertainty, and are intended to give a sense of the differences over time, but without so much detail, so additional information can be plotted on each plot. The error bars are 1-sigma limits and give an idea of the variability over periods of time, without cluttering the plot with additional dynamic information.

Because the trends appear relatively constant, it's useful to reduce the volume of information to examine the results simultaneously. To accomplish this, we average each time period, here about 8 hours. Thus, we can look where the satellites are after 1, 2, 3, etc, periods to understand how much variation is in that particular time interval. That's what the green whisker plot is showing in Fig. 6.

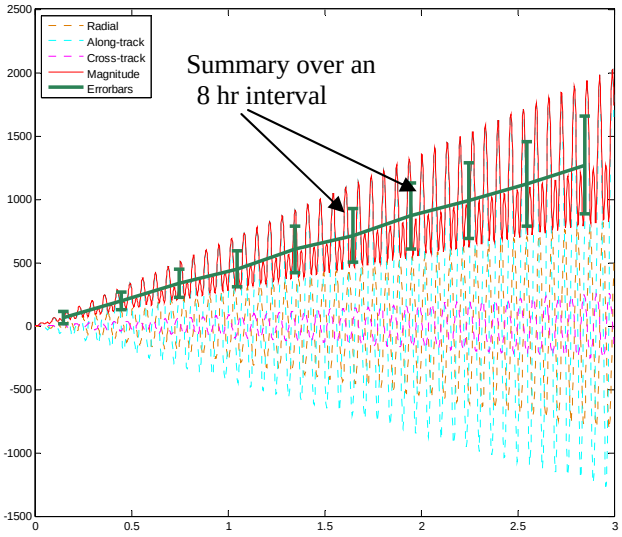

Figure 6 Positional difference of Hills and Numerical Propagation (2-body). The difference between a numerically generated orbit, and the Hills linearized approximation. Numerical integration results are shown for 2-body motion. The solid red line is the magnitude of the radial, along-track, cross-track (RAC) differences. The summary averages the variation over an interval of time (8 hours).

For two-body and perturbed motion, the LEO circular case results are shown in Fig 7. Note that the individual values are averaged over time interval (here about 8 hours) and the standard deviation is plotted as a whisker plot. This is intended to de-clutter the figure somewhat and give a sense of the variability of the error difference in each case. We also note the strong trending that is going on, giving us the opportunity to establish a trend line based on the time from epoch.

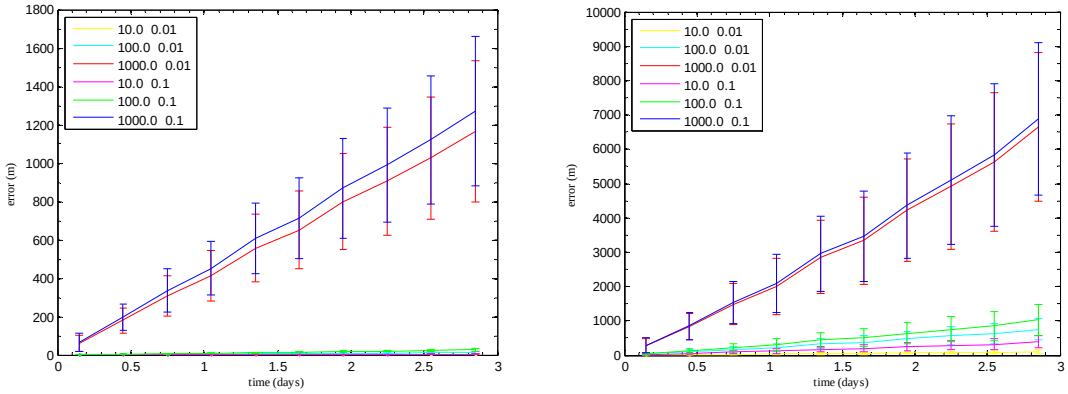

Figure 7 Positional difference of Hills and Numerical Propagation LEO Circular. The difference between a numerically generated orbit, and the Hills linearized approximation is shown. Numerical integration results are shown for 2-body and perturbed motion. The bars represent the variation during each 8 hr time interval, and the line is the average variation.

The results still appear to be reasonably linear – as we would expect because the semimajor axis is different. Thus we determined simple linear trendlines for each case. For most cases, the offset was small – although there were some exceptions, usually associated with the Perturbed cases. The rate term was our main discriminator as it was a general indicator of the error introduced by using Hills transformations for both circular and non-circular orbits. Here, the variable *t* is expressed in days.

For the Two-body cases, we have,

```
Case  10.0 m 0.01 m/s        p =   0.092672 (t) -  0.000198
Case  100.0 m 0.01 m/s       p =   4.445170 (t) -  0.031334
Case  1000.0 m 0.01 m/s      p = 406.292967 (t) -  2.322417
Case  10.0 m 0.1 m/s         p =   1.660938 (t) +  0.015021
Case  100.0 m 0.1 m/s        p =   9.267334 (t) -  0.020018
Case  1000.0 m 0.1 m/s       p = 443.249856 (t) -  2.269249
```

For the Perturbed case, we have,

```
Case  10.0 m 0.01 m/s        p =   36.019018 (t) -   3.924003
Case  100.0 m 0.01 m/s       p =  262.347641 (t) -  28.336312
Case  1000.0 m 0.01 m/s      p = 2327.870700 (t) - 265.931320
Case  10.0 m 0.1 m/s         p =  134.965546 (t) -  13.339106
Case  100.0 m 0.1 m/s        p =  356.080043 (t) -  39.620034
Case  1000.0 m 0.1 m/s       p = 2410.656200 (t) - 277.849673
```

Notice that the largest variation occurs for orbits with initial conditions that are far (1 km) away from the target satellite, which makes sense. The initial velocity displacements had much less effect, but they only went to 0.1 m/s in each axis.

Now examine a GPS-altitude, circular equatorial orbit. We also checked a GPS circular inclined orbit to make sure that the orbital elements had no effect on the transformations. For the two-body case, we would expect identical trendlines between the two cases, and we verified that in the simulation.

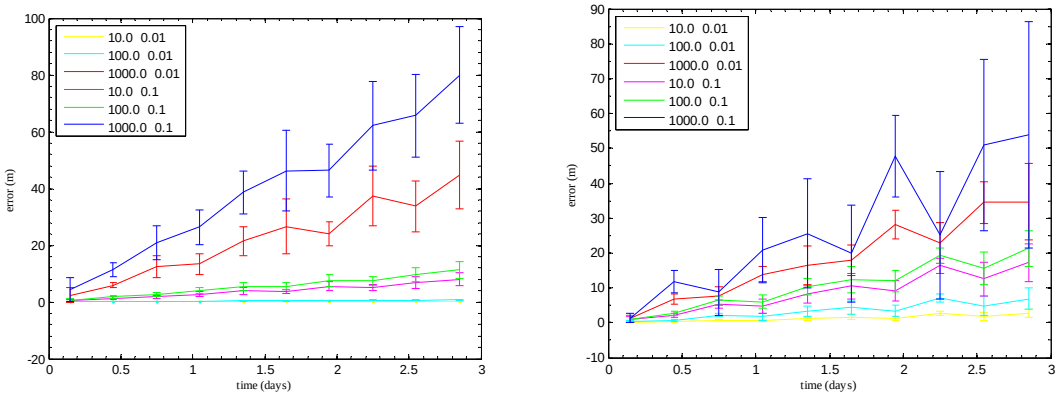

Figure 8 Positional difference of Hills and Numerical Propagation, GPS circular equatorial. The difference between a numerically generated orbit, and the Hills linearized approximation is shown. Numerical integration results are shown for 2-body and perturbed motion. The bars represent the variation during each 8 hr time interval, and the line is the average variation.

The perturbed GPS circular equatorial and inclined cases differed (as expected) due to the different positions and the different acceleration values.

For a GEO circular orbit, we have the following.

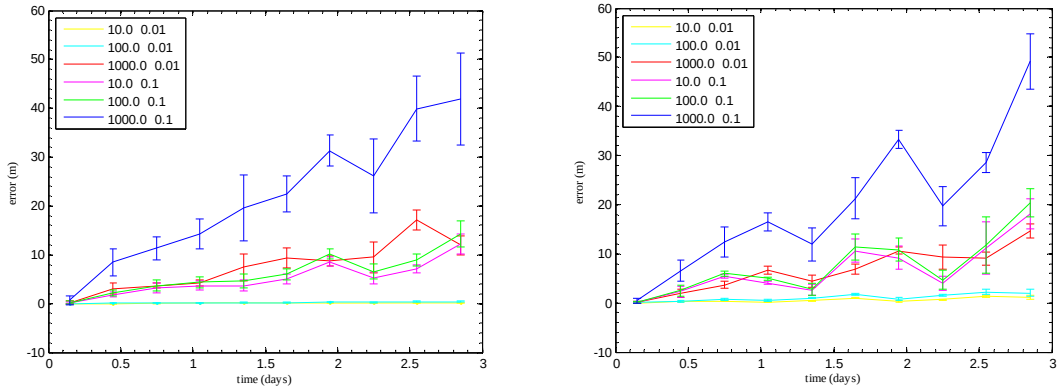

Figure 9 Positional difference of Hills and Numerical Propagation, GEO circular. The difference between a numerically generated orbit, and the Hills linearized approximation is shown. Numerical integration results are shown for 2-body and perturbed motion. The bars represent the variation during each 8 hr time interval, and the line is the average variation.

Next, we examined several satellites with small eccentricity values. These orbits should be "similar" to te circular cases because the eccentricity is relatively small in each case. For a LEO, we used a satellite with the following orbital elements. Recall that the circular LEO was at an altitude of 500 km, but also equatorial.

p km	a km	ecc	incl deg	raan deg	argp deg	nu deg	m deg
6864.9379	6864.9502	0.001336912	97.6554788	79.55466	101.98053	47.10230	46.99014

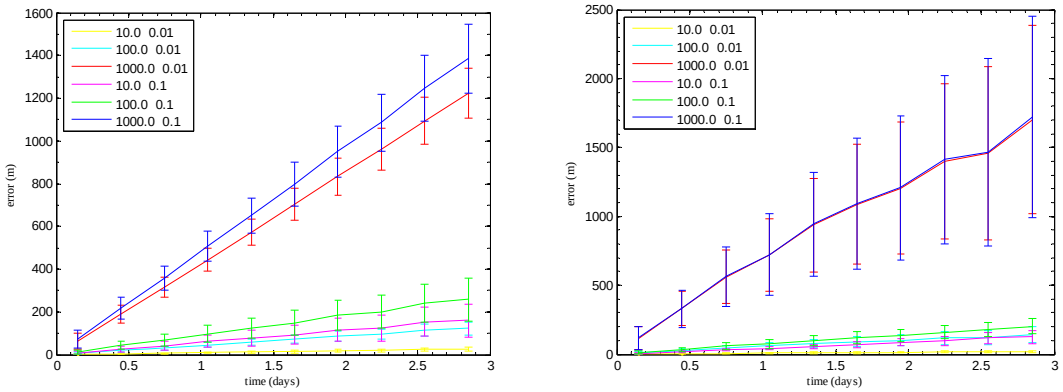

Figure 10 Positional difference of Hills and Numerical Propagation, LEO near circular. The difference between a numerically generated orbit, and the Hills linearized approximation is shown. Numerical integration results are shown for 2-body (left) and perturbed (right) motion. The bars represent the variation during each 8 hr time interval, and the line is the average variation.

Notice that the results are similar to the circular case, except for the perturbed results which we would expect due to the inclined nature of this nearly circular orbit.

For a small eccentricity GPS inclined orbit, we have the following orbital elements.

p km	a km	ecc	incl deg	raan deg	argp deg	nu deg	m deg
26565.5005	26565.8931	0.003844090	55.2474744	296.55617	188.46743	312.72094	313.04393

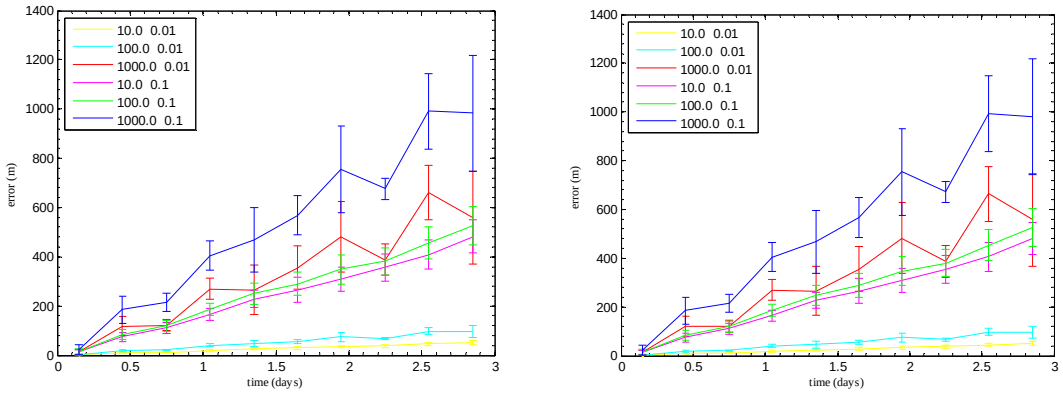

Figure 11 Positional difference of Hills and Numerical Propagation, GPS near circular inclined. The difference between a numerically generated orbit, and the Hills linearized approximation is shown. Numerical integration results are shown for 2-body (left) and perturbed (right) motion. The bars represent the variation during each 8 hr time interval, and the line is the average variation.

The GEO low inclination and near circular orbital elements are as follows.

p km	a km	ecc	incl deg	raan deg	argp deg	nu deg	m deg
42171.0268	42171.0298	0.000268282	0.0431571	78.14906	358.20236	119.41971	119.39293

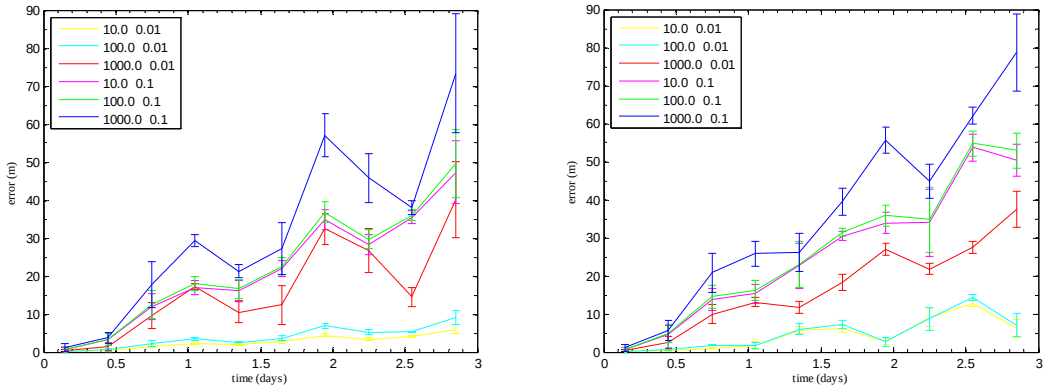

Figure 12 Positional difference of Hills and Numerical Propagation, GEO near circular. The difference between a numerically generated orbit, and the Hills linearized approximation is shown. Numerical integration results are shown for 2-body (left) and perturbed (right) motion. The bars represent the variation during each 8 hr time interval, and the line is the average variation.

If we examine more eccentric orbits, consider the following two examples. For an eccentric LEO orbit, the orbital elements are shown below. Note this is a modest eccentricity test of the eccentricity condition, which Hills equations are admittedly not designed for.

p km	a km	ecc	incl deg	raan deg	argp deg	nu deg	m deg
7982.1963	8170.9718	0.151997330	32.8682385	80.34992	117.84240	2.10039	1.52825

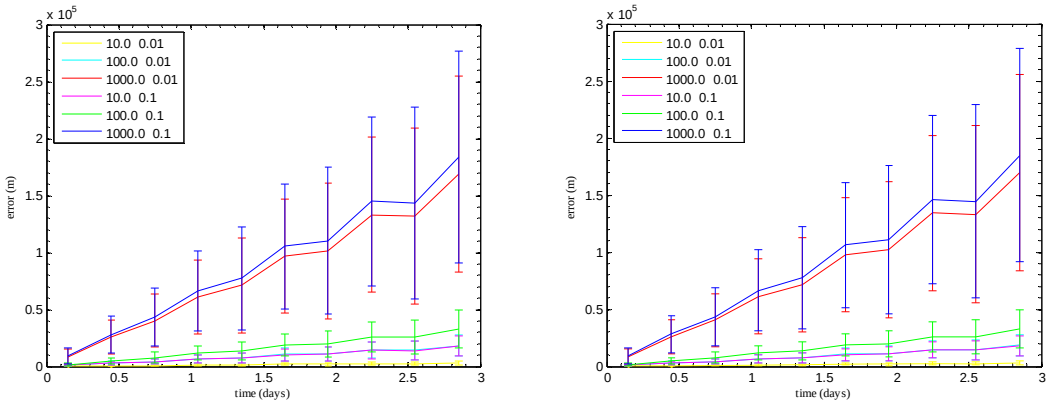

Figure 13 Positional difference of Hills and Numerical Propagation, LEO modest eccentricity. The difference between a numerically generated orbit, and the Hills linearized approximation is shown. Numerical integration results are shown for 2-body (left) and perturbed (right) motion. The bars represent the variation during each 8 hr time interval, and the line is the average variation.

For the HEO orbit, the orbital elements are shown below. Note this is a stringent test of the eccentricity condition, which Hills equations are admittedly not designed for.

p km	a km	ecc	incl deg	raan deg	argp deg	nu deg	m deg
11591.8066	25550.0883	0.739128209	62.0562099	226.25462	254.94277	263.77199	344.11265

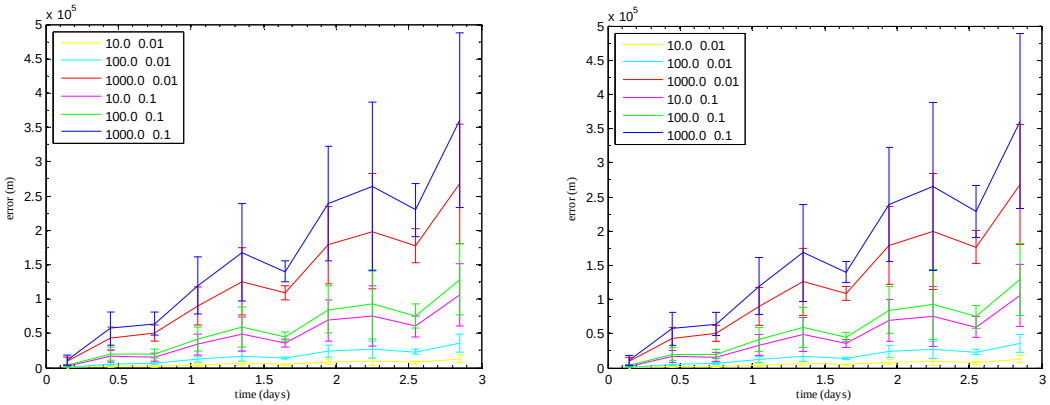

Figure 14 Positional difference of Hills and Numerical Propagation, HEO. The difference between a numerically generated orbit, and the Hills linearized approximation is shown. Numerical integration results are shown for 2-body (left) and perturbed (right) motion. The bars represent the variation during each 8 hr time interval, and the line is the average variation.

Figure 15 summarizes all the results.

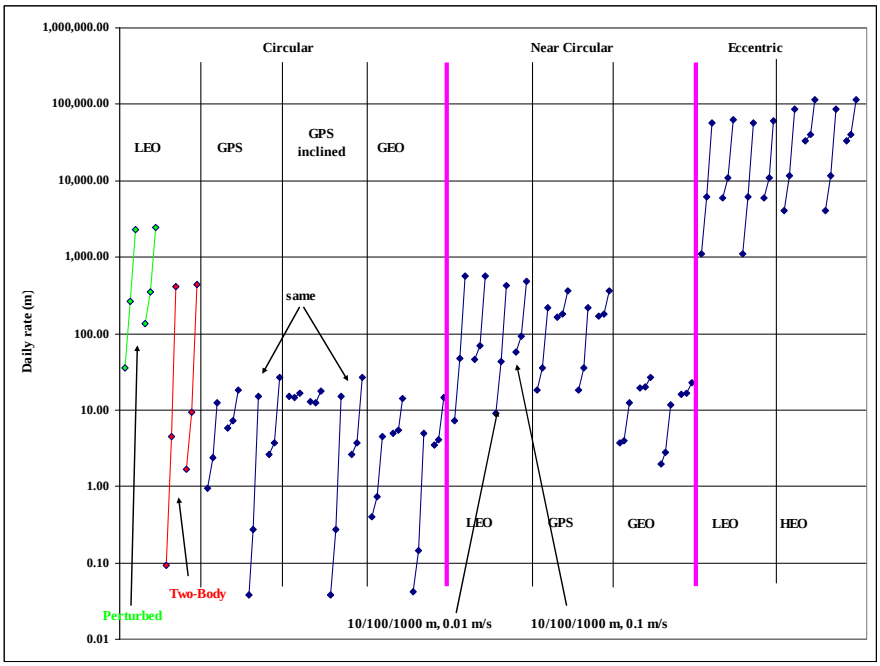

Figure 15 Rate term Positional difference of Hills and Numerical Propagation Summary. Nine cases are shown for both two-body and perturbed results. The left four cases are all circular orbits and the right five are all eccentric orbits. Each case includes 6 individual cases for initial displacements. For each case, the perturbed result is on the left and the two-body case is on the right (within each duplet). The daily rate for positional error is shown for each case. Note that the GPS circular cases are identical for the two-body equatorial and inclined cases.

We can gather a great deal of information from Fig. 15.

1. The errors in the perturbed cases were almost always greater than the two-body cases.
2. The results were always greater as the initial displacements were larger.
3. As the satellite altitude increases, the errors generally go down.

4. The errors for circular LEO orbits can be large, even when the initial displacements are not that big (100m).
5. The near circular orbits introduced noticeable errors compared to the pure circular cases.
6. Hills equations are not designed for non circular orbits, and the errors show it!

We can also examine how the transformation affects the traditional Hills diagrams. Vallado (2007:402-408) shows sample Hills plots for a variety of initial displacements. Initial *x* and *y* displacements in velocity produce elliptical, and sliding elliptical motions respectively. Figure 16 shows the behavior using perturbed motion numerical propagation, and transforming the results to Hills space. The initial *x* offset is 0.5 m/s.

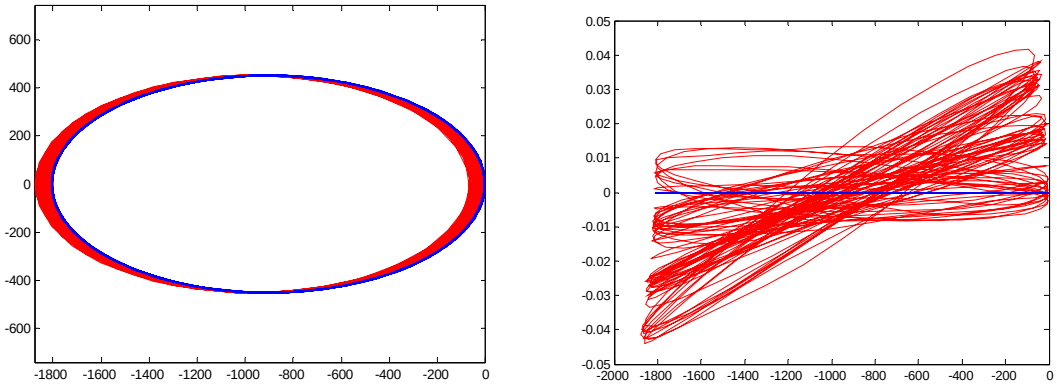

Figure 16 Hills and Perturbed Motion Hills Plot – $\dot{x}$ variation. The traditional *x* vs *y* is shown on the left, and *z* vs *y* on the right. The blue line is the Hills solution,. As time progresses (3 days) the perturbed orbit gets farther from the Hills solution, ending up nearly 400 m away at the end. The periodic motion in the z direction is also shown, and here, the Hills formulation predicts no motion, although the difference is only a fraction of a meter.

We can also examine how the results are with an initial *y* velocity displacement of 0.113 m/s.

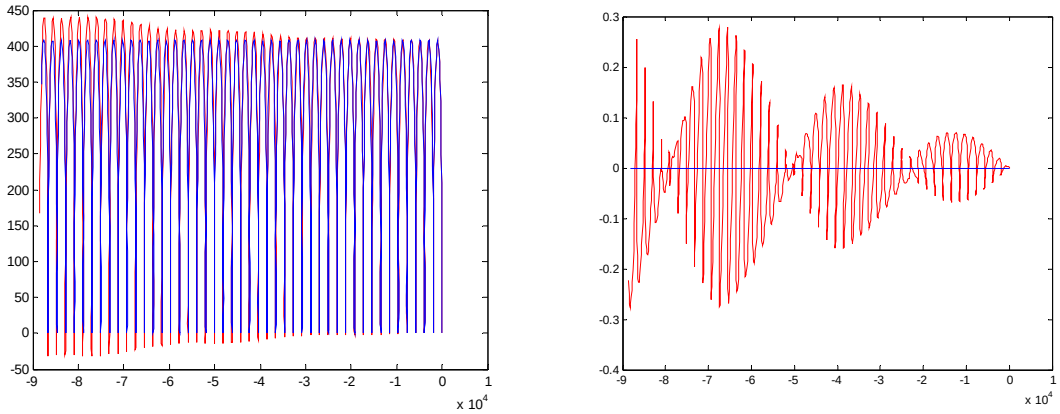

Figure 17 Hills and Perturbed Motion Hills Plot – $\dot{y}$ variation. The traditional *x* vs *y* is shown on the left, and *z* vs *y* on the right. Notice the blue line which is the Hills solution and the left figure does not have equally scaled axes so the figure is different from "usual" depictions. As time progresses (3 days) the perturbed orbit gets farther from the Hills solution, ending up nearly 400 m away at the end. The periodic motion in the *z* direction is also shown, and here, the Hills formulation predicts no motion, although the difference is less than a meter.

COVARIANCE IMPLICATIONS

The preceding analysis also applies to covariance matrices. We do not reproduce analysis that has been done for covariance propagation (Hill et al (2008, 2010), Junkins et al (1996), Sabol et al (2010), andothers). There is significant discussion about whether or not to propagate the covariance in some coordinates (or orbital elements), and then bend to the curvilinear frame, or to proceed with an Unscented Kalman Filter (UKF) approach and simply propagate in the curvilinear frame. Nevertheless, the transformations from this paper apply to any of these cases, and enables transformation to the Cartesian or curvilinear representation.

The important thing to consider is that a covariance propagated or generated from an orbit determination solution will be in a linearized frame. Consider Fig. 18. The Monte Carlo points show the true location of the covariance at the future time, but the numerically generated covariance retains a "straight" nature. The additional width of the propagated covariance accounts for some of the bending seen in the Monte Carlo representation. Notice that neither covariance is aligned with the velocity vector.

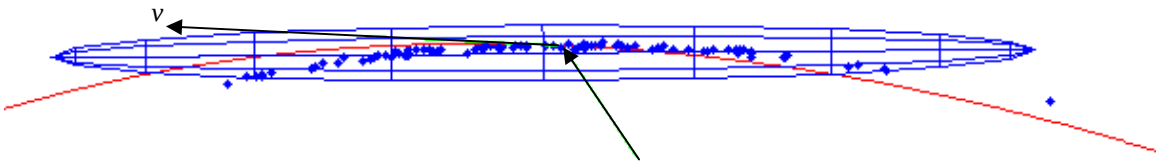

Figure 18 Covariance via Monte Carlo and Propagation. A 6 × 6 initial covariance is taken and propagated using standard numerical techniques. The resulting vector after nearly 4 days (wireframe box) is shown against Monte Carlo simulations (dots). Notice the misalignment with the velocity vector, and the additional width of the prorogated covariance.

We examined additional cases in Fig. 19 – a circular orbit, and a highly eccentric orbit. Even for a propagated covariance along a circular orbit (the blue wireframes in Fig. 19), the Hill transformation shows a significant bend from the velocity vector. The Monte Carlo results (red wireframes) show an even greater bend. Notice how the transformation moves the "ends" of the error ellipse, and how the eccentricity changes the thickness of the covariance ellipse, with greater eccentricity producing a thicker covariance. This is important should another satellite occupy the location on the bent portion of the covariance, but not on the linearized straight position.

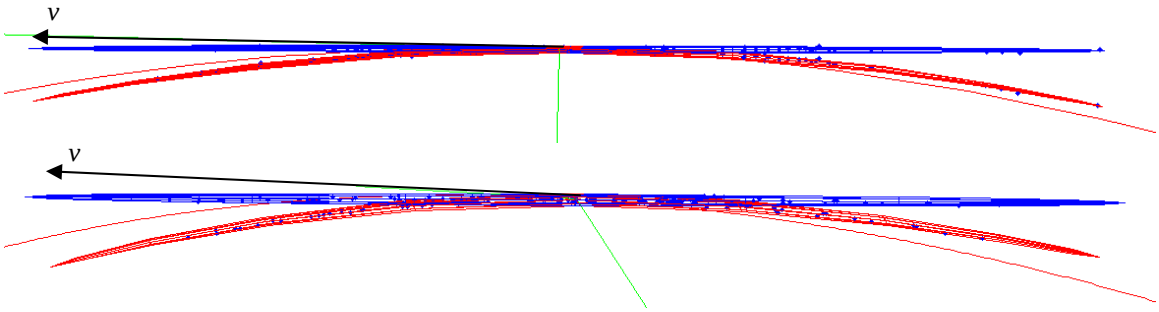

Figure 19 Covariance Representations. Three examples are shown, circular, near circular, and elliptical, from the left. The covariance is propagated through time via a UKF and Monte Carlo techniques, and then bent to a linear frame. Note the discrepancy at the ends of the ellipse and that the covariance does NOT align with the velocity vector in all cases.

Clearly any graphical representation should perform the proper beinding before displaying the results or the depcition will be extremely misleading.

CONCLUSIONS

We have shown a new formulation to convert between curvilinear and Cartesian coordinate systems. A primary benefit is to simplify the process of incorporating additional force models into Hills equations solu-

tions, but also to be general in nature to handle non-circular orbits. Errors were shown with the linearization of Hills equations for circular orbits, and several test cases demonstrated the robustness of the routines.

It appears that errors from using Hills equations can be relatively large (hundreds of meters to many kilometers) even for circular and nearly circular LEO orbits. This should be taken into account when planning missions and using these types of approaches for mission design.

We find that the covariance is not aligned with the velocity vector. This has important implications when considering covariance operations for close approaches and other operations requiring use of precise covariances. If the linearized result is used from the normal propagation of the covariance, the uncertainty will be incorrect for many regions in space.

We conclude the following about staying in the ECI frame to perform statistical operations such as conjunction analysis. First, the covariance generated from the Monte Carlo or UKF points are not centered on the unperturbed orbital position. Next, the covariance ellipse is fatter (it has a larger uncertainty and therefore a thinner density) than the EQCM ellipse. This results from trying to linearly accommodate the ECI points that clearly show a bend. Finally, we note that our transformation works only for covariances that are less than ½ an orbit revolution. Past this point, additional techniques would be needed to recover the orbital arc, and the meaning of the covariance for any actual operations would be suspect as the satellite could occupy positions in more than ½ the orbit. The resulting confidence would be extremely low.

Matlab implementations will be made available upon request as we plan additional work to further study these phenomena.

REFERENCES

Hill, K., Alfriend, and C. Sabol. 2008. Covariance-based Uncorrelated Track Association. Paper AIAA 2008-7211 presented at the AIAA/AAS Astrodynamics Specialist Conference. Honolulu, HI. August 18-21.

Hill. K., Sabol, C. and Alfriend, K.T. 2010. Comparison of Covariance-Based Track Association Approaches with Simulated Radar Data. Paper AAS 10-318 presented at the Kyle T. Alfriend Astrodynamics Symposium. Monterey, CA. May 17-19.

Hill, Keric, et al. 2010. Covariance-based Network Tasking of Optical Sensors. Paper AAS 10-150 presented at the AAS/AIAA Space Flight Mechanics Conference, February 14-17. San Diego, CA. (Also 8th USR Workshop, Maui, April 8-13, 2010, Paper S5.2).

Junkins, J.L., Akella, M.R. and Alfriend, K.T. 1996. Non-Gaussian Error Propagation in Orbital Mechanics. *Journal of the Astronautical Sciences*. Vol. 44, no. 4. pp. 541–563.

Mahalanobis, P.C. 1936. On the Generalized Distance in Statistics. Proceedings of the National Institute of Sciences of India. Vol. 2. pp. 49–55.

Park, R.S. and Scheeres, D.J. 2006. Nonlinear Mapping of Gaussian Statistics: Theory and Applications to Spacecraft Trajectory Design. *Journal of Guidance, Control, and Dynamics*. Vol. 29, no. 6. pp. 1367–1375.

Sabol, Chris, et al. 2010. Linearized Orbit Covariance Generation and Propagation Analysis via Simple Monte Carlo Simulations. Paper AAS 10-134 presented at the AAS/AIAA Space Flight Mechanics Conference, February 14-17. San Diego, CA. (Also 8th USR Workshop, Maui, April 8-13, 2010, Paper S4.1).

Seago, John H. and David A Vallado. 2010. Goodness of Fit Test for Orbit Determination. Paper AAS 10-149 presented at the AAS/AIAA Space Flight Mechanics Conference, February 14-17. San Diego, CA.

Vallado, David A. and John H. Seago. 2009. Covariance Realism. Paper AAS 09-304 presented at the AAS/AIAA Astrodynamics Specialist Conference, August 9-13. Pittsburgh, PA.

Vallado, David A. 2007. *Fundamentals of Astrodynamics and Applications*. Third Edition. Microcosm, Hawthorne, CA.

Weisstein, Eric W. June 2011. "Cylindrical Equidistant Projection." From MathWorld--A Wolfram Web Resource. http://mathworld.wolfram.com/CylindricalEquidistantProjection.html